Topological phases in non-Hermitian Aubry-André-Harper models

Qi-Bo Zeng, Yan-Bin Yang, and Yong Xu [*]

Center for Quantum Information, IIIS, Tsinghua University, Beijing 100084, People's Republic of China

Topological phases have recently witnessed rapid progress in non-Hermitian systems. Here we study a one-dimensional non-Hermitian Aubry-André-Harper (AAH) model with imaginary periodic or quasiperiodic modulations. We demonstrate that the non-Hermitian off-diagonal AAH models can host zero-energy modes at the edges. In contrast to the Hermitian case, the zero-energy mode can be localized only at one edge. Such a topological phase corresponds to the existence of a quarter winding number defined by eigenenergy in momentum space. We further find the coexistence of a zero-energy mode located only at one edge and topological nonzero-energy edge modes characterized by a generalized Bott index. In the incommensurate case, a topological non-Hermitian quasicrystal is predicted where all bulk states and two topological edge states are localized at one edge. Such topological edge modes are protected by the generalized Bott index. Finally, we propose an experimental scheme to realize these non-Hermitian models in electric circuits. Our findings add another direction for exploring topological properties in Aubry-André-Harper models.

Topological phases have become one of the most fascinating and rapidly developing research fields in condensed matter physics in the past decade, both theoretically and experimentally [1–3]. Despite being found in Hermitian systems, topological phases have recently sparked tremendous interests in non-Hermitian systems [4–47]. Such systems exist naturally or artificially due to gain or loss arising from the finite lifetime of quasiparticles [48], the interaction with environment [49,50], the engineered complex refractive index [51,52], and the engineered Laplacian in electric circuits [41,53]. A number of new topological phases have been found, such as anomalous edge modes corresponding to half a winding number in a non-Hermitian Su-Schrieffer-Heeger (SSH) model [12], Weyl exceptional rings with both nonzero Chern number and nonzero quantized Berry phase [18], and anomalous corner modes in non-Hermitian higher order topological insulators [54–56].

While there have been extensive studies of topological non-Hermitian phenomena including classification of non-Hermitian topological phases [32,44,45], the one-dimensional (1D) Aubry-André-Harper (AAH) model [57,58] has been largely overlooked and not well explored. The AAH model, a 1D system modulated by an on-site cosinusoidal potential, plays a very important role in investigating the Anderson localization and topological phases [59–72]. Specifically, the model can be mapped to a two-dimensional (2D) Hall effect system with topological edge modes [65–67]. Further generalization to an off-diagonal AAH model leads to a topological phase with zero-energy modes. Another very interesting aspect is that this model gives rise to a topological quasicrystal when the incommensurate modulation is considered [66,67].

In this Rapid Communication, we study the topological phases in a non-Hermitian off-diagonal AAH model with a purely imaginary cosinusoidal modulation and asymmetric hopping under both commensurate and incommensurate scenarios. We find that (i) non-Hermitian AAH models can host zero-energy modes at the edges. In contrast to the Hermitian counterpart, the zero-energy mode can be localized only at one edge. Such a topological phase corresponds to the existence of the structure of energy bands in momentum space enclosing a branch point of order 3 [73], in contrast to the previously discovered structure enclosing a branch point of order 1 in the SSH model [12]. That implies that starting at any quasimomentum $k = k_0$ corresponding to an energy E_0, we will return to this original energy $E(k_0)$ if we continuously follow the value of the energy $E(k)$ as the quasimomentum varies from k_0 to $k_0 + 8\pi$. This leads to a winding number being one-quarter defined by the eigenenergy. (ii) We further find the coexistence of a zero-energy mode located only at one edge and nonzero-energy edge modes. For the latter edge modes, we show that they can be characterized by a generalized Bott index in a system under open boundary conditions (OBCs). (iii) For incommensurate non-Hermitian quasicrystals, we demonstrate that both two-edge modes and all bulk states are localized at one edge, in stark contrast to the Hermitian case where all bulk states are extended and two edge modes are localized at two edges. Such topological edge modes can also be characterized by the generalized Bott index. Finally, we propose an experimental scheme with electric circuits for realizing the non-Hermitian AAH models.

Model Hamiltonian. We start by considering the following 1D non-Hermitian AAH model:

$$\hat{H} = \sum_j t(1 - \gamma + \lambda_j)\hat{c}_{j+1}^\dagger\hat{c}_j + t(1 + \gamma + \lambda_j)\hat{c}_j^\dagger\hat{c}_{j+1}, \quad (1)$$

where $\hat{c}_j^\dagger$ ($\hat{c}_j$) is the creation (annihilation) operator for a spinless particle at site j, t and γ denote the hopping strength and an asymmetric hopping strength, respectively, and $\lambda_j = i\lambda\cos(2\pi\alpha j + \delta)$ depicts an imaginary modulation with λ, α,
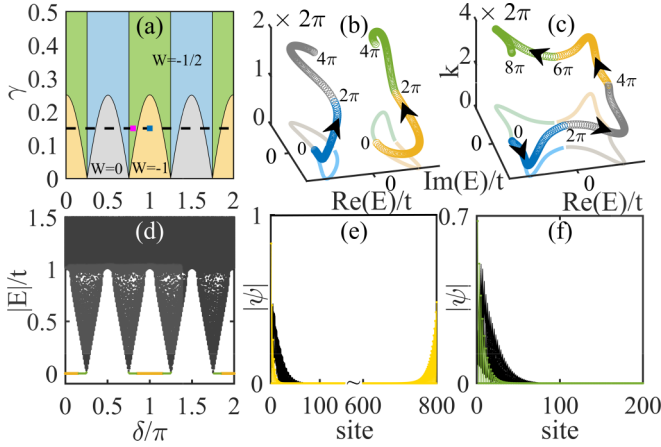
[*]yongxuphy@tsinghua.edu.cn

FIG. 1. (a) Phase diagram with respect to δ and γ, where the yellow, green, blue, and gray areas represent the phases with $(W, N_e) = (-1, 2), (-1/2, 1), (-1/2, 0), (0, 0)$, respectively. In the region with $W = -1/2$, we find $W_E = 1/4$. Complex energy spectra versus k and their projection in the $k = 0$ plane for (b) $\delta = \pi$, $\gamma = 0.15$ and (c) $\delta = 0.8\pi$, $\gamma = 0.15$ corresponding to the blue and pink squares in (a), respectively. We also label the position of k where $k = 2m\pi$ with m being an integer. (d) Absolute values of the eigenenergy versus δ under OBCs for $\gamma = 0.15$ as indicated by the dashed black line in (a). The green and yellow lines at zero energy depict the one zero-energy eigenstate located only at the left edge and two zero-energy eigenstates located at both edges, respectively. (e),(f) Amplitudes of wave functions with parameters indicated by the blue and pink squares in (a), respectively. The black lines denote the bulk states while the yellow and green lines denote the zero-energy edge states. Here, the lattice size $L = 800$, $\lambda = 1$, and $\alpha = 1/4$.

and δ being real parameters. When α is a rational number such that $\alpha = p/q$ with p and q being relatively prime positive integers, the modulation is periodic with q being its period, whereas the modulation becomes quasiperiodic, when α is an irrational number.

To determine the eigenenergy and eigenstates of the system under OBCs, we write the Hamiltonian as $\hat{H} = \hat{c}^\dagger H \hat{c}$ where $\hat{c} = (\hat{c}_1 \quad \hat{c}_2 \quad \cdots \quad \hat{c}_L)$ with L being the number of sites and diagonalize the Hamiltonian $H^\dagger$ and H allowing us to obtain both the left and right eigenstates $|\Psi_n^L\rangle$ and $|\Psi_n^R\rangle$ which satisfy $H^\dagger |\Psi_n^L\rangle = E_n^* |\Psi_n^L\rangle$ and $H|\Psi_n^R\rangle = E_n |\Psi_n^R\rangle$ (E_n is the corresponding eigenenergy), respectively. In the commensurate case, the Hamiltonian is translational invariant with respect to q sites under periodic boundary conditions. As a result, we can write the Hamiltonian in momentum space as $\hat{H} = \sum_k \hat{c}_k^\dagger H(k) \hat{c}_k$ where $\hat{c}_k = (\hat{c}_{1k} \quad e^{-ik/q} \hat{c}_{2k} \quad \cdots \quad e^{-i(q-1)k/q} \hat{c}_{qk})$ with $k \in [0, 2\pi]$ and $H(k)_{mn} = \delta_{mn-1} t_m + \delta_{m-1n} t_n' + \delta_{m1} \delta_{nq} t_q' e^{-ik} + \delta_{mq} \delta_{n1} t_q e^{ik}$ with $t_j = t(1 + \gamma + \lambda_j)$ and $t_j' = t(1 - \gamma + \lambda_j)$. Note that we have scaled the quasimomentum k so that $k \in [0, 2\pi]$. The left and right eigenvectors in momentum space $|\Psi_n^L(k)\rangle$ and $|\Psi_n^R(k)\rangle$ can be obtained by diagonalizing the matrix $H^\dagger(k)$ and $H(k)$, respectively.

Zero-energy modes in the commensurate AAH model. Let us first consider the commensurate modulation. To show the topological features, we first consider the simplest case with $\alpha = 1/4$. In Fig. 1(a), we map out the topological phase

diagram with respect to δ and γ, showing four distinct topological phases characterized by (W, N_e), where W and N_e denote the winding number of the Hamiltonian in momentum space and the number of zero-energy edge eigenstates, respectively. These four phases correspond to $(W, N_e) = (-1, 2), (-1/2, 1), (-1/2, 0), (0, 0)$, which will be elaborated on in the following discussion.

Since the 1D system for a fixed δ respects the sublattice symmetry [74,75], $H(k)$ can be transformed into an off-diagonal block form [75]: $H(k) \rightarrow [0 \ h_1(k); h_2(k) \ 0]$, and the winding number for each block is defined as [32] $w_{1,2} = \int_0^{2\pi} \frac{dk}{2\pi i} \partial_k \ln \det h_{1,2}(k)$. We can further define the winding number of the system as $W \equiv (w_1 - w_2)/2$ [32]. In the Hermitian case, $h_2 = h_1^\dagger$ leading to $w_1 = -w_2$ and thus W has to equal an integer. However, the non-Hermitian term breaks this relation so that W can be a half integer [32]. This occurs in our system with $W = -1/2$ [see Fig. 1(a)]. For a system with two energy bands, such as the SSH model, if $W = \pm 1/2$, we have $w_1 = n$ and $w_2 = n \pm 1$ with n being an integer and thus $h_1 \propto e^{in\theta_1(k)}$ and $h_2 \propto e^{i(n\pm1)\theta_2(k)}$, where $\theta_\nu(k)$ ($\nu = 1, 2$) changes continuously from $\theta_\nu(k_0)$ to $\theta_\nu(k_0) + 2\pi$ as k varies from k_0 to $k_0 + 2\pi$. Since the eigenenergy is $E_k = \pm\sqrt{-h_1(k)h_2(k)} \propto e^{in(\theta_1+\theta_2)/2} e^{i\theta_2/2}$, implying that one ends up with the other energy $-E$ starting from one energy E as k varies from k_0 to $k_0 + 2\pi$.

However, in our system, we find that when $W = -1/2$, all four of these energy bands are connected [see Fig. 1(c)], so that a state needs to travel across the Brillouin zone four times to return. To describe such features, we define a winding number for a separable energy band E_n as

$$W_{E_n} = \frac{1}{2m\pi} \int_0^{2m\pi} dk \, \partial_k \arg[E_n(k) - E_B] \quad (2)$$

with respect to a base energy E_B, where $E_n(k) = E_n(k + 2m\pi)$ with m being the smallest integer so that this relation is satisfied. For the non-Hermitian SSH model involving a branch point of order 1, $W_E = 1/2$. However, in our system when $W = -1/2$, we find $W_E = 1/4$. Further calculation of the Berry phase $C_1 = \int_0^{2m\pi} dk \langle \Psi_n^L(k)|\partial_k \Psi_n^R(k)\rangle / \langle \Psi_n^L(k)|\Psi_n^R(k)\rangle$ as k varies from 0 to 8π shows that $C_1 \bmod 2\pi = \pi$ in the region with $W = -1/2$ [18]. Interestingly, in the region with $W = -1$ and $W = 0$ and $\gamma \neq 0$, we see that each separable energy band encloses a branch point of order 1, yielding $W_{E_1} = W_{E_2} = 1/2$ with respect to the corresponding base energies inside the rings [see Fig. 1(b)].

Under OBCs, we show that when $W = -1$, there appear two zero-energy edge states located at two edges as shown in Fig. 1(e). While this is similar to the Hermitian case, different properties arise that all bulk states are localized at the left edge when $\gamma > 0$ due to the non-Hermitian skin effects arising from the asymmetric hopping. More interestingly, when $W = -1/2$, we find a region (green) where there is only one zero-energy eigenstate located only at the left edge [see Fig. 1(f)]. In fact, the system exhibits a zero-energy exceptional point with a zero-energy eigenstate and a zero-energy generalized eigenstate, where the Hamiltonian becomes defective. The number of zero-energy eigenstates and generalized zero-energy eigenstates are determined by $N - \text{rank}(H)$ with
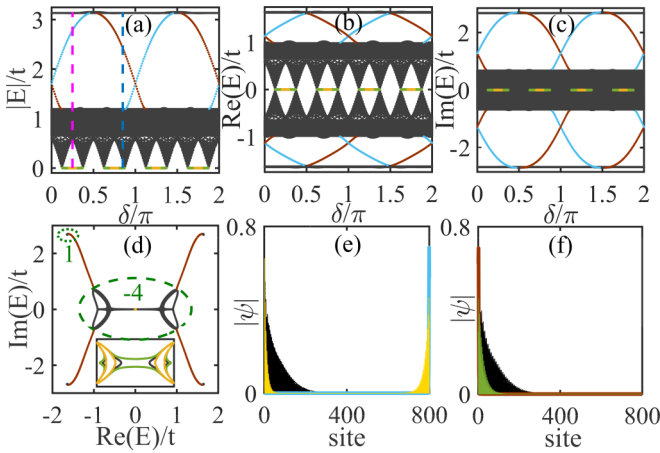
FIG. 2. (a) Absolute values, (b) real parts, and (c) imaginary parts of complex eigenenergy versus δ under OBCs. The green and yellow lines denote the one and two zero-energy edge states, respectively. The cyan and brown lines represent the nonzero-energy edge states located at the left and right edges, respectively. (d) Energy spectra in the complex energy plane for all δ under OBCs. The brown lines represent the nonzero-energy edge states located at two edges. The inset presents energy spectra of the Hamiltonian in momentum space for three different δ values: 0.05π (black), 0.12π (green), and 0.25π (yellow). The green numbers show the generalized Bott index for the states inside the corresponding circles. (e),(f) Amplitudes of eigenstates for $\delta = \pi/4$ and 0.85π corresponding to the dashed pink and blue lines in (a), respectively. The black lines depict the bulk states. In (e), the yellow (cyan) lines correspond to two zero-energy edge states (nonzero-energy edge states). In (d), the green (brown) line denotes the zero-energy (nonzero-energy) edge mode. Here, $L = 800$, $\lambda = 2$, $\alpha = 1/8$, and $\gamma = 0.05$.

$N = L$ and rank(H) − rank(H^2), respectively. These two values change from 2 to 1 and 0 to 1, respectively, as γ varies from the yellow region to the green one.

In addition, we see that there exists a region (blue) where despite $W = −1/2$ and $W_E = 1/4$, no zero-energy modes emerge, showing that the winding number defined in momentum space cannot be used to characterize the zero-energy modes. This arises from the dramatic change of the bulk wave functions as boundary conditions are changed [27]. To restore the bulk-edge correspondence, we need to use the wave functions under OBCs to calculate the winding number. Let us follow the method proposed in Refs. [30,76] and calculate the det($H(\beta) − EI) = 0$ where I is an identity matrix and $H(\beta) = H(e^{ik} \rightarrow \beta)$ with the Hamiltonian H in momentum space [75]. This equation gives us two solutions β_1 and β_2 for each E satisfying $\beta_1 \beta_2 = \prod_{j=1}^q t'_j / \prod_{j=1}^q t_j$. For the bulk states, $|\beta_1| = |\beta_2| = r$. This leads to a generalized Bloch Hamiltonian $\tilde{H} = H(e^{ik} \rightarrow re^{ik})$ so that calculation of the winding number of this Hamiltonian gives us the phase boundary for the existence of zero-energy modes. In fact, this new Hamiltonian gives the same winding number as the case without γ. For $\gamma = 0$, we do not find any skin effects so that the bulk-edge correspondence is preserved, implying that the gap closing of the energy bands in momentum space with respect to δ signals whether zero-energy edge modes appear. We find that the gap closes when $\delta = (2j + 1)\pi/4$

with $j = 0, 1, 2, 3$ and zero-energy edge modes emerge when $|\sin\delta| < |\cos\delta|$ as shown in Fig. 1.

In the general case, when $q = 4m + 2$ (m being an integer and $4m$ being prime to p) instead of a multiple of 4, we find that the energy spectrum of $\tilde{H}$ is gapless with the presence of zero-energy eigenstates for every $\delta \in [0, 2\pi]$ [75], indicating the absence of the zero-energy edge modes in such cases [77]. When $q = 4m$, we have proved that the spectrum of $\tilde{H}$ is gapless when $\delta = (2n + 1)\pi/(4m)$ with $n = 0, 1, \ldots, 4m − 1$ (suppose $m > 0$) [75]. When $\gamma = 0$, it is proved that a gapped region can appear, showing that the topologically nontrivial zero-energy modes can exist [75]. In other cases, for instance, when q is an odd number, there is no sublattice symmetry and thus the zero-energy states cannot be protected.

Coexistence of distinct types of edge modes in the commensurate AAH model. The non-Hermitian AAH model also exhibits a peculiar feature that the single zero-energy mode can coexist with other topological nonzero-energy edge modes (see Fig. 2). Specifically, Fig. 2 shows that there exist two regions with one and two zero-energy edge states, respectively. In the former region, $W_E = 1/4$ for the eigenstates in momentum space. Besides the zero-energy states, we find other edge modes inside a gap, reminiscent of chiral edge modes in a Chern insulator if δ is viewed as a quasimomentum. In the complex energy plane for all δ, we observe five separable bands with four lines connecting four bands outside to one at the center; these four lines correspond to the edge states.

When $\gamma > 0$, we find that all bulk states are localized at the left edge, implying that we need to use the wave functions obtained under OBCs to characterize the "chiral" edge states. Here, we generalize the Bott index by defining it as (see details in the Supplemental Material [75]; see also Refs. [78–81] therein)

$$\text{Bott} = \frac{1}{2\pi}\text{Im Tr} \ln U_y U_x U_y^\dagger U_x^\dagger, \qquad (3)$$

where $U_{a,mn} = \langle\Psi_m^L|e^{2\pi i\hat{a}/L_a}|\Psi_n^R\rangle$ with $a = x, y$ and $\hat{x}$ and $\hat{y}$ denoting the position operators along x or y, respectively, and L_a labeling the size of the system along the corresponding direction. Additionally, $|\Psi_n^R\rangle$ and $|\Psi_m^L\rangle$ represent the right and left eigenvectors in a separable band, respectively. To calculate the Bott index, we map our system into a 2D Harper model [84]. Transforming this Hamiltonian along y to the form in momentum space exactly gives us the Hamiltonian (1) if k_y is replaced with δ. This allows us to calculate the Bott index of H_{2D} under periodic (open) boundary conditions along y (x) to obtain the topological invariant of our system. We find that for the five separable bands, the Bott index is $−4$ for the central band and 1 for each of the other four bands at the corners of the complex energy plane [see Fig. 2(d)], demonstrating that the edge states are topologically protected. We note that, with OBCs, while there appear edge states connecting the separable bands, their presence does not affect our results.

Non-Hermitian quasicrystals. When α is irrational, the non-Hermitian AAH model becomes quasiperiodic, and the imaginary modulation is incommensurate with lattice spacings, leading to a quasicrystal. Similar to the commensurate scenario, in Fig. 3(a), we illustrate the energy spectrum in the complex energy plane for all δ from 0 to 2π
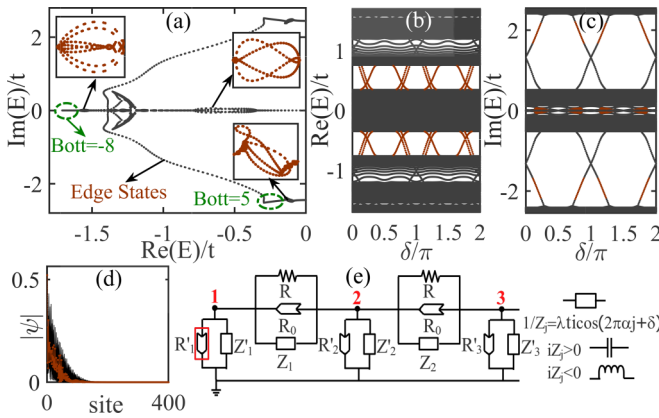
FIG. 3. (a) Energy spectra in the complex energy plane for the non-Hermitian quasicrystal. The insets plot the zoomed-in figures of the edge states inside the corresponding energy gaps. Real (b) and imaginary (c) parts of the complex energies. (d) Amplitudes of the bulk states (black lines) and edge states (brown lines) for $\delta = \pi/4$. For the figures above, $L = 610$, $\lambda = 2$, $\alpha = (\sqrt{5} - 1)/2$, and $\gamma = 0.1$. (e) Schematics of the electric circuit configuration for realizing the non-Hermitian AAH model. The electric element in the red box denotes a negative impedance converter with current inversion (INIC) [82,83]. R'_j and R_0 denote the resistance of the INICs, the sign of which depends on the orientation of the INIC. R represents the impedance of a resistor, and Z_j and Z'_j that of a capacitor or a inductor. The rectangle electric element represents a capacitor or inductor determined by the value of the hopping as shown in the right figures.

for $\alpha = (\sqrt{5} - 1)/2$. The figure exhibits rich band structures. Apparently, there are two separable bands with the imaginary value around ± 2.5. They are connected by the edge states (denoted by the brown lines) to the band with real energies. For each of these two bands, there is also a minigap within which four edge states reside (see the insets). For the band with real energies, there exist a gap and a minigap with four and eight edge states inside, respectively. These edge states can also be observed when the energy spectrum is projected to the real or imaginary part.

Remarkably, we further find that all bulk states are localized at the left edge when $\gamma \neq 0$ and all edge states are located at the left edge when γ is sufficiently large, in stark contrast to the Hermitian case, as shown in Fig. 3(d). We note that the localization of the bulk states is caused by the non-Hermitian

skin effect instead of the Anderson localization. Since the bulk states are sensitive to the boundary conditions, we cannot apply a twisted boundary condition to calculate the Chern number as the Hermitian case [66]. Instead, we can still calculate the Bott index using the wave functions obtained under OBCs. We find that the Bott index for each separable band equals the number of edge states inside the gap. For instance, the Bott index of the band with the imaginary value around ± 2.5 and the real value smaller than -0.1 is 5, protecting five edge states coming from this band [see Fig. 3(a)].

Experimental realizations. Recently, electric circuits have been demonstrated to be a powerful platform to simulate topological phenomena, such as the SSH model [53], Weyl semimetals [85], higher order topological insulators [86], and topological amorphous metals [81]. Here, we propose an experimental scheme with electric circuits for realizing the non-Hermitian AAH models [see Fig. 3(e) and [75]]. We can achieve the required Laplacian so that $J = -(EI + H)$ by choosing appropriate impedances for these electric devices [87]. The edge states can be observed by measuring the two-point impedance between two nodes which diverges as $E + E_n = 0$ as we vary E.

In summary, we have demonstrated that for the commensurate non-Hermitian off-diagonal AAH model, there exist zero-energy states localized at the edges. In contrast to the Hermitian case, the edge states can be localized only at one edge. Such a topological phase corresponds to the emergence of a quarter winding number defined by eigenenergy in momentum space. We further find that the zero-energy edge modes can coexist with nonzero-energy edge modes protected by the generalized Bott index. For the incommensurate case, topological non-Hermitian quasicrystals with edge modes are predicted. These edge modes can be characterized by the generalized Bott index. Our study can also be extended to the diagonal AAH models. Very recently, the Anderson localization phase transition associated with the $\mathcal{PT}$ symmetry breaking in the diagonal AAH model has been suggested [88,89]. Our findings pave the way for further studies on topological properties in non-Hermitian Aubry-André-Harper models.

[1] M. Z. Hasan and C. L. Kane, Rev. Mod. Phys. **82**, 3045 (2010).

[2] X.-L. Qi and S.-C. Zhang, Rev. Mod. Phys. **83**, 1057 (2011).

[3] N. P. Armitage, E. J. Mele, and A. Vishwanath, Rev. Mod. Phys. **90**, 015001 (2018).

[4] M. S. Rudner and L. S. Levitov, Phys. Rev. Lett. **102**, 065703 (2009).

[5] K. Esaki, M. Sato, K. Hasebe, and M. Kohmoto, Phys. Rev. B **84**, 205128 (2011).

[6] C.-E. Bardyn, M. A. Baranov, C. V. Kraus, E. Rico, A. İmamoğlu, P. Zoller, and S. Diehl, New J. Phys. **15**, 085001 (2013).

[7] A. V. Poshakinskiy, A. N. Poddubny, L. Pilozzi, and E. L. Ivchenko, Phys. Rev. Lett. **112**, 107403 (2014).

[8] J. M. Zeuner, M. C. Rechtsman, Y. Plotnik, Y. Lumer, S. Nolte, M. S. Rudner, M. Segev, and A. Szameit, Phys. Rev. Lett. **115**, 040402 (2015).

[9] S. Malzard, C. Poli, and H. Schomerus, Phys. Rev. Lett. **115**, 200402 (2015).

[10] M. S. Rudner, M. Levin, and L. S. Levitov, arXiv:1605.07652.

[11] P. San-Jose, J. Cayao, E. Prada, and R. Aguado, Sci. Rep. **6**, 21427 (2016).

[12] T. E. Lee, Phys. Rev. Lett. **116**, 133903 (2016).

[13] J. González and R. A. Molina, Phys. Rev. Lett. **116**, 156803 (2016).

[14] A. K. Harter, T. E. Lee, and Y. N. Joglekar, Phys. Rev. A **93**, 062101 (2016).

[15] Q. B. Zeng, B. Zhu, S. Chen, L. You, and R. Lü, Phys. Rev. A **94**, 022119 (2016).

[16] S. Weimann, M. Kremer, Y. Plotnik, Y. Lumer, S. Nolte, K. G. Makris, M. Segev, M. C. Rechtsman, and A. Szameit, Nat. Mater. **16**, 433 (2017).

[17] D. Leykam, K. Y. Bliokh, C. Huang, Y. D. Chong, and F. Nori, Phys. Rev. Lett. **118**, 040401 (2017).

[18] Y. Xu, S.-T. Wang, and L.-M. Duan, Phys. Rev. Lett. **118**, 045701 (2017).

[19] H. Menke and M. M. Hirschmann, Phys. Rev. B **95**, 174506 (2017).

[20] L. Xiao, X. Zhan, Z. H. Bian, K. K. Wang, X. Zhang, X. P. Wang, J. Li, K. Mochizuki, D. Kim, N. Kawakami, W. Yi, H. Obuse, B. C. Sanders, and P. Xue, Nat. Phys. **13**, 1117 (2017).

[21] S. Lieu, Phys. Rev. B **97**, 045106 (2018).

[22] A. A. Zyuzin and A. Y. Zyuzin, Phys. Rev. B **97**, 041203(R) (2018).

[23] A. Cerjan, M. Xiao, L. Yuan, and S. Fan, Phys. Rev. B **97**, 075128 (2018).

[24] V. M. Martinez Alvarez, J. E. Barrios Vargas, and L. E. F. Foa Torres, Phys. Rev. B **97**, 121401(R) (2018).

[25] H. Zhou, C. Peng, Y. Yoon, C. W. Hsu, K. A. Nelson, L. Fu, J. D. Joannopoulos, M. Soljačić, and B. Zhen, Science **359**, 1009 (2018).

[26] C. Yin, H. Jiang, L. Li, R. Lü, and S. Chen, Phys. Rev. A **97**, 052115 (2018).

[27] Y. Xiong, J. Phys. Commun. **2**, 035043 (2018).

[28] H. Shen, B. Zhen, and L. Fu, Phys. Rev. Lett. **120**, 146402 (2018).

[29] F. K. Kunst, E. Edvardsson, J. C. Budich, and E. J. Bergholtz, Phys. Rev. Lett. **121**, 026808 (2018).

[30] S. Yao and Z. Wang, Phys. Rev. Lett. **121**, 086803 (2018).

[31] S. Yao, F. Song, and Z. Wang, Phys. Rev. Lett. **121**, 136802 (2018).

[32] Z. Gong, Y. Ashida, K. Kawabata, K. Takasan, S. Higashikawa, and M. Ueda, Phys. Rev. X **8**, 031079 (2018).

[33] K. Kawabata, K. Shiozaki, and M. Ueda, Phys. Rev. B **98**, 165148 (2018).

[34] K. Takata and M. Notomi, Phys. Rev. Lett. **121**, 213902 (2018).

[35] Y. Chen and H. Zhai, Phys. Rev. B **98**, 245130 (2018).

[36] X. Qiu, T.-S. Deng, Y. Hu, P. Xue, and W. Yi, iScience **20**, 392 (2019).

[37] Z. Yang and J. Hu, Phys. Rev. B **99**, 081102 (2019).

[38] H. Wang, J. Ruan, and H. Zhang, Phys. Rev. B **99**, 075130 (2019).

[39] A. Cerjan, S. Huang, M. Wang, K. P. Chen, Y. Chong, and M. C. Rechtsman, Nat. Photonics **13**, 623 (2019).

[40] L. Jin and Z. Song, Phys. Rev. B **99**, 081103 (2019).

[41] K. F. Luo, J. J. Feng, Y. X. Zhao, and R. Yu, arXiv:1810.09231.

[42] F. K. Kunst and V. Dwivedi, Phys. Rev. B **99**, 245116 (2019).

[43] Y. Xu, Front. Phys. **14**, 43402 (2019).

[44] K. Kawabata, K. Shiozaki, M. Ueda, and M. Sato, Phys. Rev. X **9**, 041015 (2019).

[45] H. Zhou and J. Y. Lee, Phys. Rev. B **99**, 235112 (2019).

[46] K. Kawabata, S. Higashikawa, Z. Gong, Y. Ashida, and M. Ueda, Nat. Commun. **10**, 297 (2019).

[47] L. Herviou, J. H. Bardarson, and N. Regnault, Phys. Rev. A **99**, 052118 (2019).

[48] V. Kozii and L. Fu, arXiv:1708.05841.

[49] C. M. Bender and S. Boettcher, Phys. Rev. Lett. **80**, 5243 (1998).

[50] C. M. Bender, Rep. Prog. Phys. **70**, 947 (2007).

[51] Z. H. Musslimani, K. G. Makris, R. El-Ganainy, and D. N. Christodoulides, Phys. Rev. Lett. **100**, 030402 (2008).

[52] L. Feng, R. El-Ganainy, and L. Ge, Nat. Photonics **11**, 752 (2017).

[53] C. H. Lee, S. Imhof, C. Berger, F. Bayer, J. Brehm, L. W. Molenkamp, T. Kiessling, and R. Thomale, Commun. Phys. **1**, 39 (2018).

[54] T. Liu, Y.-R. Zhang, Q. Ai, Z. Gong, K. Kawabata, M. Ueda, and F. Nori, Phys. Rev. Lett. **122**, 076801 (2019).

[55] E. Edvardsson, F. K. Kunst, and E. J. Bergholtz, Phys. Rev. B **99**, 081302 (2019).

[56] X.- W Luo and C. Zhang, Phys. Rev. Lett. **123**, 073601 (2019).

[57] S. Aubry and G. André, Ann. Isr. Phys. Soc. **3**, 133 (1980).

[58] P. G. Harper, Proc. Phys. Soc., London, Sect. A **68**, 874 (1955).

[59] S. Ostlund, R. Pandit, D. Rand, H. J. Schellnhuber, and E. D. Siggia, Phys. Rev. Lett. **50**, 1873 (1983).

[60] M. Kohmoto, Phys. Rev. Lett. **51**, 1198 (1983).

[61] S. Das Sarma, S. He, and X. C. Xie, Phys. Rev. Lett. **61**, 2144 (1988).

[62] S. Das Sarma, S. He, and X. C. Xie, Phys. Rev. B **41**, 5544 (1990).

[63] J. Biddle, B. Wang, D. J. Priour, Jr., and S. Das Sarma, Phys. Rev. A **80**, 021603(R) (2009).

[64] J. Biddle and S. Das Sarma, Phys. Rev. Lett. **104**, 070601 (2010).

[65] L.-J. Lang, X. Cai, and S. Chen, Phys. Rev. Lett. **108**, 220401 (2012).

[66] Y. E. Kraus, Y. Lahini, Z. Ringel, M. Verbin, and O. Zilberberg, Phys. Rev. Lett. **109**, 106402 (2012).

[67] Y. E. Kraus and O. Zilberberg, Phys. Rev. Lett. **109**, 116404 (2012).

[68] S. Ganeshan, K. Sun, and S. Das Sarma, Phys. Rev. Lett. **110**, 180403 (2013).

[69] X. Cai, L.-J. Lang, S. Chen, and Y. Wang, Phys. Rev. Lett. **110**, 176403 (2013).

[70] F. Liu, S. Ghosh, and Y. D. Chong, Phys. Rev. B **91**, 014108 (2015).

[71] J. Wang, X.-J. Liu, G. Xianlong, and H. Hu, Phys. Rev. B **93**, 104504 (2016).

[72] Q. B. Zeng, S. Chen, and R. Lü, Phys. Rev. B **94**, 125408 (2016).

[73] T. Needham, *Visual Complex Analysis* (Oxford University Press, New York, 1999).

[74] C.-K. Chiu, J. C. Y. Teo, A. P. Schnyder, and S. Ryu, Rev. Mod. Phys. **88**, 035005 (2016).

[75] See Supplemental Material at http://link.aps.org/supplemental/10.1103/PhysRevB.101.020201 for further information on the generalized Bloch Hamiltonian and the proof for the condition for the existence of topological zero modes. The definition for the winding number and the generalized Bott index as well as the details of the experimental realization in electric circuits are also included there.

[76] K. Yokomizo and S. Murakami, Phys. Rev. Lett. **123**, 066404 (2019).

[77] Here the generalized Bloch Hamiltonian $\tilde{H}$ is used instead of $H(k)$ because of the breakdown of the bulk-edge correspondence when $\gamma \neq 0$.

[78] T. A. Loring and M. B. Hastings, Europhys. Lett. **92**, 67004 (2010).

[79] D. Toniolo, arXiv:1708.05912.

[80] Y. Ge and M. Rigol, Phys. Rev. A **96**, 023610 (2017).

[81] Y.-B. Yang, T. Qin, D.-L. Deng, L.-M. Duan, and Y. Xu, Phys. Rev. Lett. **123**, 076401 (2019).

[82] W.-K. Chen, *The Circuits and Filters Handbook*, 3rd ed. (CRC Press, Boca Raton, FL, 2009).

[83] T. Hofmann, T. Helbig, C. H. Lee, M. Greiter, and R. Thomale, Phys. Rev. Lett. **122**, 247702 (2019).

[84] $H_{2D} = \sum_{j_x, j_y} t(1+\gamma)\hat{c}^\dagger_{j_x, j_y}\hat{c}_{j_x+1, j_y} + t(1-\gamma)\hat{c}^\dagger_{j_x+1, j_y}\hat{c}_{j_x, j_y} + t\frac{i\lambda}{2}[e^{-i2\pi\alpha j_x}(\hat{c}^\dagger_{j_x, j_y+1}\hat{c}_{j_x+1, j_y} + \hat{c}^\dagger_{j_x+1, j_y+1}\hat{c}_{j_x, j_y}) + \text{H.c.}].$

[85] Y. Lu, N. Jia, L. Su, C. Owens, G. Juzeliūnas, D. I. Schuster, and J. Simon, Phys. Rev. B **99**, 020302(R) (2019).

[86] S. Imhof, C. Berger, F. Bayer, J. Brehm, L. W. Molenkamp, T. Kiessling, F. Schindler, C. H. Lee, M. Greiter, T. Neupert, and R. Thomale, Nat. Phys. **14**, 925 (2018).

[87] $1/R = t$, $1/R_0 = t\gamma$, $1/Z_j = \lambda ti \cos(2\pi\alpha j + \delta)$, $1/R'_1 = 1/R'_L = t(1-\gamma) + \text{Re}(E)$ and $1/Z'_1 = -1/Z_1 - \text{Im}(E)$, $1/Z'_L = -1/Z_{L-1} - \text{Im}(E)$, and $1/R'_j = 2t + \text{Re}(E)$ and $1/Z'_j = -1/Z_{j-1} - 1/Z_{j+1} - \text{Im}(E)$ when $1 < j < L$.

[88] S. Longhi, Phys. Rev. Lett. **122**, 237601 (2019).

[89] H. Jiang, L.-J. Lang, C. Yang, S.-L. Zhu, and S. Chen, Phys. Rev. B **100**, 054301 (2019).